JTSE - Journal of Tropical Science and Engineering
Volume 1, Issue 2, June 2026
https://doi.org/10.58334/jtse.vol.001.795

Microstructure, mechanical properties and corrosion behavior of nickel-aluminum bronze fabricated by wire-arc additive manufacturing

Shabunina Zhanna Sergeevna[(1)], Uglunts Tigran Vladimirovich[(1,2)], Silkin Alexey Olegovich[(1)], Mendagaliev Ruslan Valisovich[(1)], Shabunina Sofia Sergeevna[(1)], Cao Nhat Linh[(3)]✉, Nguyen Van Chi[(3)], Khalaman Vyacheslav Vyacheslavovich[(4)], Gazizova Marina Yurievna[(1)], Klimova-Korsmik Olga Gennadievna[(1)]

[(1)] *World-Class Research Center "Advanced Digital Technologies", State Marine Technical University, Saint-Petersburg, Russian Federation*

[(2)] *Peter the Great Polytechnic University, Saint-Petersburg, Russian Federation*

[(3)] *Coastal Branch, Joint Vietnam-Russia Tropical Science and Technology Research Center, Khanh Hoa, Vietnam*

[(4)] *Zoological Institute of the Russian Academy of Sciences, Saint-Petersburg, Russian Federation*

✉**Corresponding author**

E-mail: cnlinh0812@gmail.com

ORCID: 0000-0002-5493-092X

Abstract

This paper presents the first study of the corrosion behavior of nickel-aluminum bronze CuAl9Ni5 produced by the wire-arc additive manufacturing (WAAM-CMT) method in tropical seawater, and the effect of heat treatment on it. To improve the mechanical properties, a two-stage heat treatment was performed: quenching at 900°C followed by aging at 400°C. Metallographic analysis revealed that this treatment results in a refined and uniform distribution of phase formations, compared to the original Widmanstätten structure. This resulted in a significant increase in hardness and strength. In parallel, laboratory electrochemical tests were conducted in synthetic seawater, and long-term field tests were performed at the Nha Trang offshore station (Vietnam) for 2544 hours (approximately 106 days). All samples, including heat-treated ones, demonstrated high corrosion resistance, with a corrosion rate in the laboratory of below 0.04 mm/year. The damage was only superficial. The obtained results prove that the combination of WAAM technology and heat treatment modes makes it possible to create large-sized products (e.g., propellers) from CuAl9Ni5 bronze with an optimal combination of mechanical properties and exceptional resistance to marine corrosion.

Keywords

Wire-arc additive manufacturing, nickel-aluminum bronze, electrochemical corrosion, corrosion testing in seawater, heat treatment, microstructure, mechanical properties

Introduction

Additive manufacturing, as a modern method for producing metallic structures, offers several advantages over traditional manufacturing techniques and has attracted significant attention from researchers worldwide (Mendagaliev *et al.*, 2020; Korsmik *et al.*, 2020). One of the promising methods for producing high-precision near-net-shape components is WAAM, based on the layer-by-layer fabrication of parts by melting metal wire using the heat of an arc source. This technology is characterized by high productivity, efficient material utilization, cost-effectiveness, and simplicity of equipment (Singh & Khanna, 2021). These advantages make WAAM relevant to various high-tech industries, such as shipbuilding, aerospace, rocketry, railway transport, nuclear energy, and many others (Srivastava *et al.*, 2023). As a result, numerous studies have been devoted to WAAM using aluminum, titanium alloys, and steels (Sarıkaya *et al.*, 2024; Guo *et al.*, 2024; Liao *et al.*, 2024). Among the materials, aluminum bronzes (Cai *et al.*, 2022) alloyed with small amounts of Ni, Fe, and Si occupy a special place. These alloys possess low density, high specific strength, and excellent corrosion resistance in seawater. Such properties make nickel-aluminum bronzes an excellent material for producing components for the marine industry, such as propellers (Chalasani & Mohammadi, 2023; Govindaraj *et al.*, 2021; Shakil *et al.*, 2024) and hybrid marine equipment parts (Chalasani *et al.*, 2020; Cai *et al.*, 2023; Liu *et al.*, 2024).

In seawater, copper alloys can form a relatively dense film that provides corrosion protection; however, sand and gravel inevitably damage operational equipment such as pumps and propellers, breaking the protective layer formed by corrosion products (Cai *et al.*, 2023). NAB alloys fabricated via WAAM exhibit superior mechanical properties and corrosion resistance compared to their cast counterparts (Zhang *et al.*, 2024). Nevertheless, their heterogeneous microstructure may negatively influence corrosion behavior in seawater. It has been

Received: November 04, 2025 | Revised: December 01, 2025 | Accepted: January 29, 2026

reported that corrosion pits were observed in the β- and κ-phases following immersion in sodium chloride solution. Poonburri et al. also found that the β-phase experienced severe corrosion and exfoliation, as it contained higher concentrations of Al and Mn and had a lower electron work function than the α-phase. Furthermore, fine Cu_3Mn_2Al precipitates within the β-phase induced galvanic corrosion, further accelerating exfoliation (Song *et al.*, 2022).

It can be expected that the optimal heat treatment for WAAM-NAB parts will differ from that of conventionally cast forms due to substantial differences in the initial microstructures. For instance, depending on the heat treatment temperature, substantial fresh precipitation of κ-phases may occur in WAAM-NAB, which significantly influences both mechanical performance and corrosion behavior (Chalasani *et al.*, 2020). At moderate cooling rates, such as those associated with arc-based processes, the microstructure typically consists of Widmanstätten α-phase and various κ-phases, which become more refined as the cooling rate increases. This results in enhanced tensile properties in WAAM-produced NAB, including a 17% increase in yield strength and a 90% improvement in ductility compared to the cast alloy (Orzolek *et al.*, 2022).

The solidification process in WAAM primarily depends on the heat input during welding and the cooling rate. Common strategies for managing thermal accumulation in WAAM processes include optimizing the deposition path, adjusting the welding current, increasing the travel speed, and implementing auxiliary measures such as bypass current and hot wire feeding (Liu *et al.*, 2024). The cooling rate in WAAM can be regulated by controlling the interlayer dwell time and modifying convective heat transfer between the deposited layer and the surrounding environment. The corrosion behavior of NAB alloys produced by WAAM may differ from that of their cast counterparts. However, the protective passivation film's formation and the WAAM-fabricated NAB's corrosion resistance remain insufficiently studied. Given the industrial importance of NAB corrosion characteristics, further investigation into the corrosion behavior of WAAM-produced NAB is necessary (Liu *et al.*, 2024; Xu *et al.*, 2023).

Since bronze alloys are widely used in seawater environments, this form of corrosion constitutes a significant mode of material degradation that adversely affects the durability and reliability of structures and equipment across various industries (Chalasani *et al.*, 2019). Corrosion in marine environments develops due to the combined effects of an aggressive medium (saltwater) and biofouling of the alloy surface (biocorrosion). This type of corrosion poses a serious threat to critical metallic components operating in seawater, such as propellers (Kayvandarian *et al.*, 2024). Marine corrosion also represents a substantial challenge for shipbuilding, the oil and gas industry, port facilities, and coastal infrastructure. The synergistic impact of saltwater and marine organisms on metallic surfaces greatly accelerates localized corrosion processes compared to exposure to saltwater alone. In most laboratory tests and studies, a 3.5% NaCl solution is commonly used to simulate simplified seawater conditions (Arcos *et al.*, 2024). In such an environment, the corrosion resistance of most alloys tends to be higher than under actual service conditions. Therefore, comprehensive laboratory and full-scale field testing at climatic stations provides the most significant scientific and practical value.

This study investigates the formation of the microstructure and the mechanical properties of $CuAl_9Ni_5$ aluminum bronze fabricated using the WAAM-CMT method. In this work, the microstructure of the samples was studied, and corrosion tests were conducted in a tropical field exposure for 2544 hours, with a direct quantitative comparison made with lab tests for WAAM $CuAl_9Ni_5$. Additionally, particular heat treatment windows suitable for WAAM-CMT $CuAl_9Ni_5$ were researched.

Materials and methods

Material and sample preparation

The wire used in the study was CastoMag 45752 ($CuAl_9Ni_5$), produced by Castolin Eutectic, with a diameter of 1.2 mm. The chemical composition of the wire was analyzed using a scanning

electron microscope (SEM, TESCAN Mira 3) equipped with an energy-dispersive spectroscopy (EDS) detector (Advanced Ultim Max 65) operated at an accelerating voltage of 20 kV. The initial raw material used for manufacturing was $CuAl_9Ni_5$ wire, with a diameter of 1.2 mm. The results of the EDS analysis of the wire are presented in Table 1.

Table 1. Elemental composition of $CuAl_9Ni_5$ wire based on EDS analysis (wt.%)

Element	Cu	Al	Ni	Mn	Fe	Si
CastoMag Wire 45752	Bal.	8.14	4.10	1.44	3.32	0.41
Standard deviation	–	0.14	0.22	0.39	0.16	0.12

Samples for the study were fabricated using a WAAM-CMT system, the schematic of which is shown in Figure 1a. The deposition was carried out under a high-purity argon shielding gas flow of 15 L/min, with a current of 180 A and a tool travel speed of 8 mm/s. After each layer was applied, there was a pause for air cooling to 300°C. The X-axis offset was - 4.74 mm, and the Z-axis offset was - 2 mm. The deposited samples are shown in Figure 1b; the sample dimensions were 200 × 100 × 20 mm.

A SNOL 40/1200 laboratory furnace was used for the heat treatment of the samples. The specimens fabricated via the WAAM-CMT method were placed in a preheated furnace and, in the case of quenching, held at 900°C for 1 hour, followed by water cooling. For aging, the samples were held at 400°C for 3 hours (regime AA-2) and 5 hours (regime AA-3), followed by air cooling.

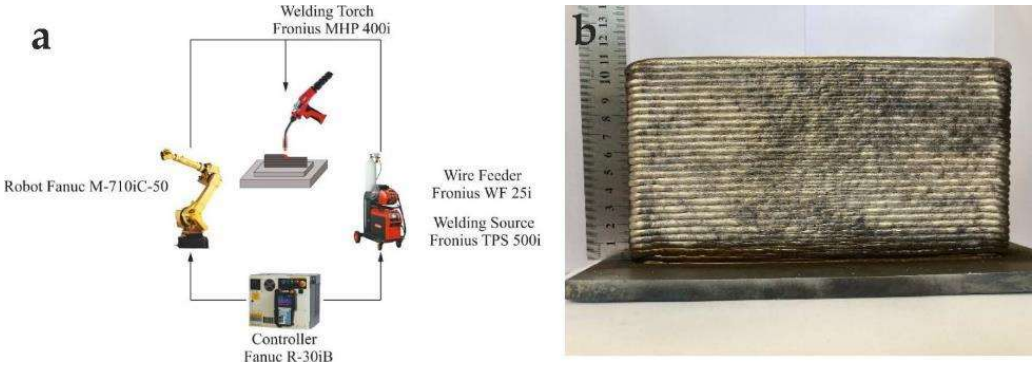

Figure 1. Schematic diagram: (a) Schematic diagram of the WAAM-CMT setup; (b) WAAM-fabricated sample made of $CuAl_9Ni_5$ aluminum bronze.

Methods

Samples for microstructural study were ground on SiC paper with a grain size up to 2500, after which they were polished with diamond suspensions. For macro- and microstructural study, samples were etched in a 50% HNO_3 solution. The microstructure was studied using a Leica DMi8 optical microscope and Axalit software.

For the microstructural study using EBSD analysis, polished samples were subjected to 24 hours of vibratory polishing using a SiO_2 suspension. EBSD analysis was performed using a TESCAN Mira 3 scanning electron microscope equipped with a C-Nano detector and Aztec software.

Tensile tests were conducted according to Standard Test Methods for Tension Testing of Metallic Materials to determine the mechanical properties of the samples obtained after printing and processing. Static tensile mechanical tests were performed on a Shimadzu AGS-X 100 kN testing machine at a strain rate of 1.0×10^{-3} s^{-1} at room temperature. Specimens are made according to ASTM E8.

The samples for the corrosion test were prepared as disks with a diameter of 13 mm, featuring a copper wire brazed to the reverse side. The samples were embedded in epoxy electrical

insulating resin, and the section of the copper wire exposed to the electrolyte during the experiment was insulated by applying a wax-rosin mixture. The working surface of the samples was ground using SiC paper, polished with diamond suspensions, and degreased with ethyl alcohol. The corrosion test was performed using potentiodynamic polarization in a solution simulating seawater. The composition of the solution is provided in Table 2.

Table 2. Composition of the test solution simulating seawater.

Component	NaCl	$MgCl_2 \cdot 6H_2O$	Na_2SO_4	$CaCl_2$	KCl	$NaHCO_3$	H_3BO_3
g/L	22.00	9.70	3.70	1.00	0.65	0.20	0.023

An AP-40X potentiostat-galvanostat and a LOIP LT-205a circulating thermostat were used to conduct the corrosion test. The test was performed in an open, thermostated, three-electrode cell at a temperature of 30°C, with a solution volume of 300 mL. An Ag/AgCl electrode with a standard potential of −202 mV was used as the reference electrode, and a graphite electrode was the auxiliary electrode. Polarization was carried out at a scan rate of 0.5 mV/s from -200 mV to +750 mV vs. Ag/AgCl. The pH of the solution was 7.5 ± 1. The method described in ASTM G59 and G102 was used to calculate the uniform corrosion rate. For each state of material (Initial, AA-2, AA-3), three identical samples were used for electrochemical testing.

Full-scale corrosion tests were conducted with the Joint Vietnam-Russia Tropical Science and Technology Research Center. The tests were carried out at a marine field climatic station located in the city of Nha Trang. Samples measuring 15 × 15 × 100 mm were cleaned with a brush, rinsed with distilled water, and degreased with alcohol before testing. The mass of the samples before and after exposure was recorded using analytical balances with an accuracy of 0.1 mg. The samples were mounted on special racks and fully immersed in seawater from August 12, 2024, to November 26, 2024, for a total of 2544 hours. The corrosion exposure stand is shown in Figure 2.

The corrosion rate was calculated using the following formula:

$$CR1 = \frac{\Delta m}{S \times t} \left(\frac{g}{m^2 \times h}\right) \quad (1)$$

The following formula was used to convert the results to units of mm/year:

$$CR2 = \frac{K \times \Delta m}{S \times t \times \rho} \left(\frac{mm}{year}\right) \quad (2)$$

where Δm - mass loss (g), S - the surface area of the sample (cm^2), t - exposure time (h), ρ - alloy density (g/cm^3), K - conversion factor ($mm \cdot cm^3$)/($g \cdot cm^2 \cdot h$), with $K = 8.76$.

Figure 2. Test stand for full-scale seawater exposure.

Results

Microstructural analysis

Figure 3 presents the microstructure of the alloy following WAAM-CMT processing. The as-built (Initial) alloy exhibits a microstructure consisting of more finely dispersed α-phase

grains with relatively small regions of β-phase between them, along with isolated κ-phase inclusions that are predominantly precipitated at α/β phase boundaries. The fractions of β and κ phases in the Initial state are markedly lower than in AA-2 and AA-3; κ-phase particles are smaller without heat treatment, which is attributed to the high solidification and cooling rates inherent to WAAM. After heat treatment (AA-2), the microstructure undergoes appreciable changes: the fractions of β and κ phases increase, and the α-phase grains coarsen. With more extended aging (AA-3), κ-phase particles become larger and more numerous (Figure 3), and the β-phase fraction also increases (Figure 4).

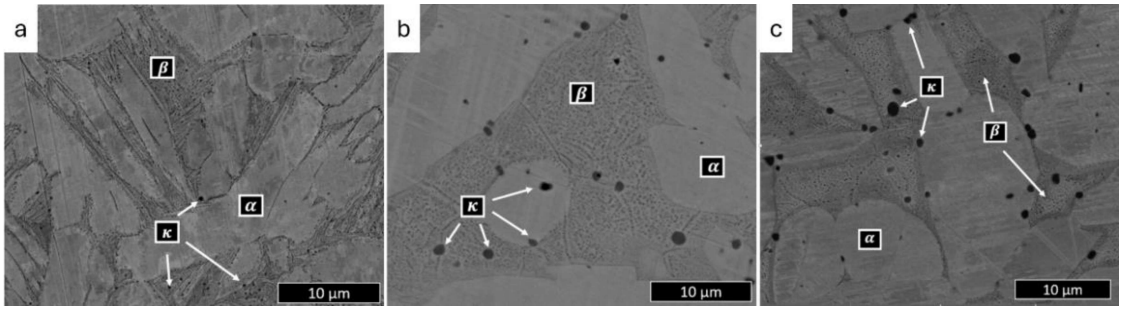

Figure 3. The microstructure of the alloy following WAAM-CMT processing: (a) as-built condition (Initial); (b) after AA-2 heat treatment; (c) after AA-3 heat treatment.

Figure 4 presents the results of the EBSD analysis of the samples in the as-built condition and after heat treatment. In the as-built state, the average grain area of α-phase was 178 µm^2. The grain size increased after heat treatment, with average grain areas reaching 378 µm^2 and 381 µm^2 for the AA-2 and AA-3 heat treatment regimes, respectively.

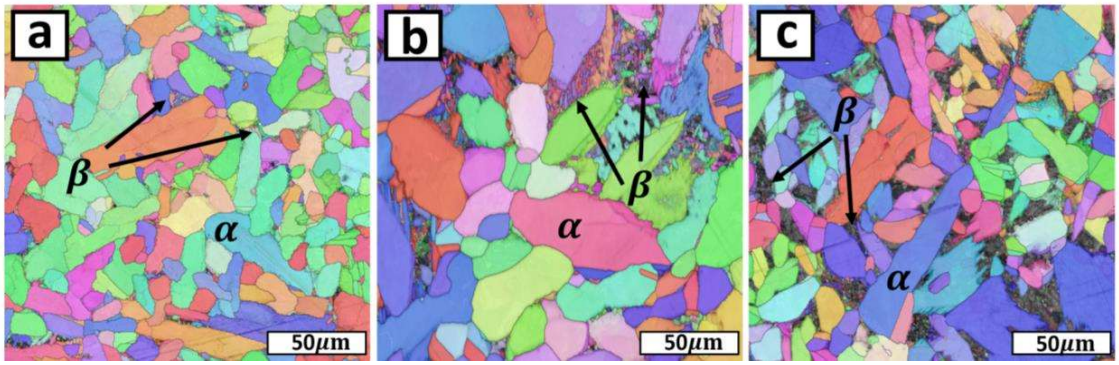

Figure 4. EBSD analysis results of the samples: (a) as-built condition; (b) after AA-2 heat treatment; (c) after AA-3 heat treatment.

Figure 5 shows elemental distribution maps for the AA-3 specimen, and Figure 6 presents EDS analysis of the structural constituents. The alloy consists of cells of an α-phase solid solution of Al, Ni, Fe, Si, and Mn in a copper matrix. The solid-solution cells are surrounded by a eutectoid constituent of the β-phase, which, as indicated by the elemental maps, is enriched in Al and Ni and depleted in Cu relative to the α-phase (Figure 5). Owing to its low solubility in copper, iron precipitates at the cell boundaries of the α and β phases and within β-phase regions as spherical intermetallic κ-phase inclusions with an average area of 0.4 µm^2 (Kayvandarian *et al.*, 2024). Figure 6 and Table 3 show that κ-phase particles are enriched in Fe, Ni, and Si compared with the α and β phases.

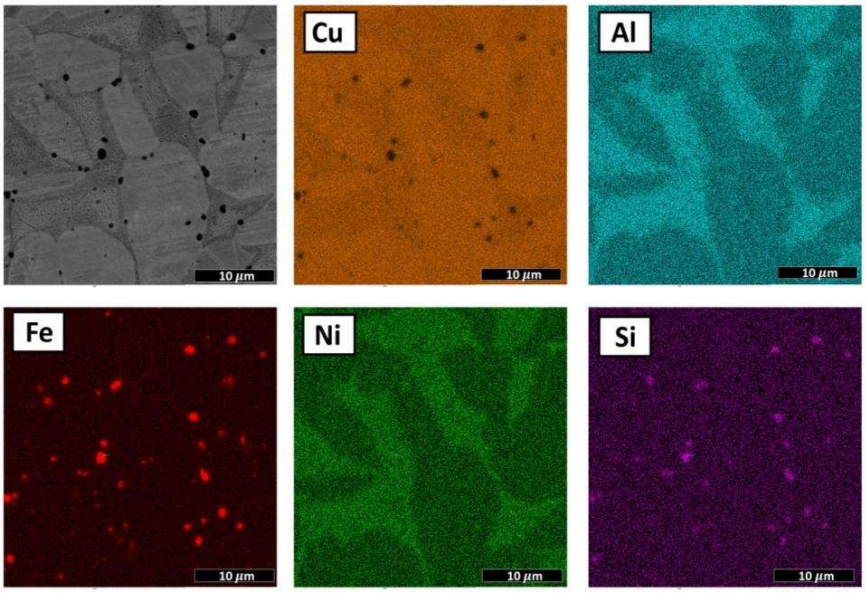

Figure 5. Elemental distribution maps for AA-3.

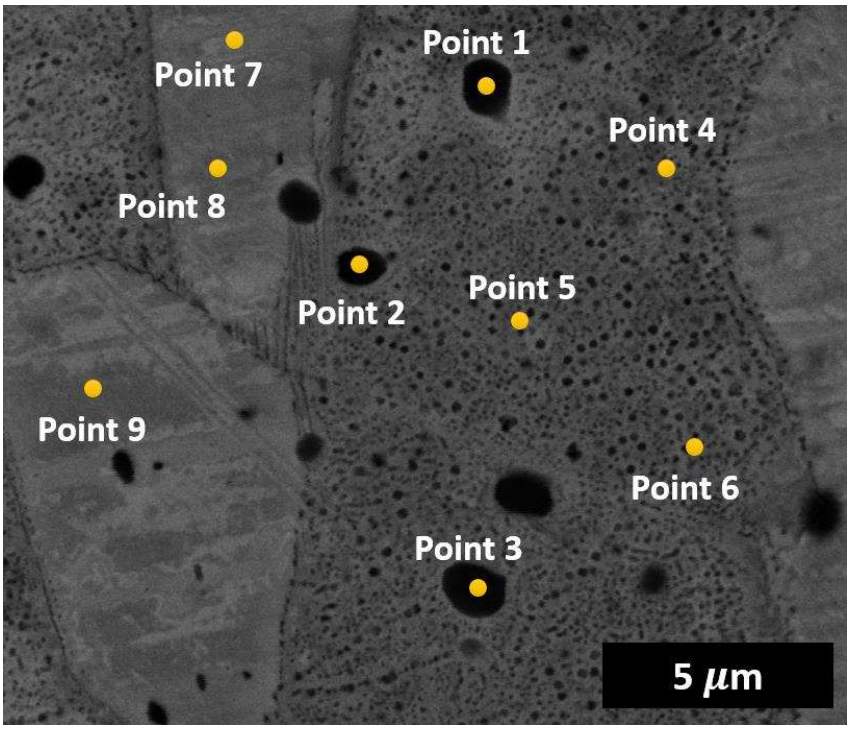

Figure 6. EDS analysis of the structure components of sample AA-3 in wt.%.

Table 3. EDS elemental composition (wt.%) at points 1-9 marked in Figure 6

Points	Cu	Al	Ni	Fe	Si	Mn
1-3	30.82	9.06	8.00	47.27	2.83	2.02
4-6	79.40	10.56	5.93	2.61	-	1.51
7-9	84.15	7.74	3.81	2.98	-	1.30

Mechanical properties

The results of the microhardness measurements are presented in Table 4. According to the obtained data, the investigated aging durations did not reduce microhardness, indicating that the applied heat treatment conditions did not cause over-aging of the material. An increase in holding time resulted in higher microhardness values, with the AA-2 and AA-3 conditions yielding similar hardness values of 222 HV and 225 HV, respectively. These values exceed the as-built microhardness by 30% and 32%. Therefore, the AA-2 and AA-3 heat treatment regimes were selected for subsequent mechanical testing.

Table 4 presents the results of the tensile mechanical tests. As shown in the table, the AA-2 and AA-3 heat treatment conditions resulted in increases in yield strength of 22% and 26%, respectively, and an increase in ultimate tensile strength of 12%, while maintaining satisfactory levels of elongation.

Table 4. Tensile and microhardness measurement results

State	Test direction	σ_{YS}, MPa	σ_{UTS}, MPa	Elongation, %	Microhardness, HV
Initial	X	235±11	603±15	43.1±2.1	171±12
AA-2	X	286±9	673±7	30.2±1.2	222±7
AA-3	X	295±8	677±4	27.0±1.3	225±6

Electrochemical corrosion test

The time evolution of the open-circuit potential (E_{ocp}) indicates that all specimens are sufficiently stable under the test conditions, with E_{ocp} fluctuations not exceeding 10 mV after 10 minutes from the start (Figure 7a). The E_{ocp} values for all conditions differ only marginally (Table 5).

Table 5 Electrochemical corrosion test results

State	E_{ocp}, mV	E_{cor}, mV	$i_{cor} \times 10^{-3}$, A/cm^2	E_{op}, mV	$i_{op} \times 10^{-3}$, A/cm^2	E_p, mV	$i_f \times 10^{-3}$, A/cm^2
Initial	-221±5	-234±5	1.92±0.3	93±5	14.60±0.8	162±5	7.96±0.4
AA-2	-218±7	-231±5	2.35±0.5	76±5	14.77±0.7	140±5	7.71±0.7
AA-3	-224±5	-236±5	2.03±0.3	73±5	13.34±0.7	124±5	9.01±0.5

E_{op} - passivation onset potential, i_{op} - passivation onset current, E_p - passivation potential, i_p - passivation current, i_f - current at potential E = 750 mV

Potentiodynamic polarization curves of the Al-Cu-Ni alloy in the synthetic seawater solution are shown in Figure 7. The corrosion current density and corrosion potential were obtained by approximating Tafel regions in semi-logarithmic coordinates (Table 5). The corrosion potentials, similar to Eocp, are close in value; notably, AA-2 exhibits a higher E_{cor} (-231 mV). In contrast, for AA-3, where the aging time was increased from 3 to 5 h, Ecor decreases to -236 mV (Figure 8). The corrosion current densities, which reflect the corrosion rate, differ slightly. However, the lowest corrosion rate corresponds to the as-built specimen, and AA-3 dissolves more slowly than AA-2.

The anodic branch of the polarization curves was additionally examined for a more detailed analysis of the dissolution behavior and an assessment of the corrosion resistance of the Al-Cu-Ni alloy (Figure 7b). All investigated

conditions exhibit a passive region. The increase in current in the anodic region marks the onset of dissolution: for the as-built specimen, this occurs at -37 mV, and for the heat-treated states AA-2 and AA-3 at -42 mV and -48 mV, respectively. It should be noted that the variation of these potentials with heat-treatment regime follows the same trend as the corrosion potential. The stage of active dissolution is followed by a period of passivation. The potential at which a decrease in current density is observed is referred to as the passivation onset potential, E_{op}, and the potential at which the dissolution rate sharply decreases, and the alloy enters the passive state is the complete passivation potential, E_p. For the as-built alloy, passivation began at E_{op} = 93 mV with a current density of $i_{op} = 14.60\times10^{-3}$ A/cm^2. In contrast, heat treatment enabled the onset of passivation at lower Eop values regardless of aging time (Table 5). The transition to the passive state in the as-built specimen also occurred at a higher Ep than in the AA-2 and AA-3 samples (Table 5). It is worth noting that AA-3, after the longer aging time, exhibits a narrower and less intense passivation peak than AA-2 (3 h aging) and the as-built state, indicating a reduced dissolution rate (Figure 7b). Shortening the aging time to 3 h intensifies dissolution, and the most pronounced passivation peak is observed on the anodic branch; accordingly, the passivation-onset current density is highest for AA-2, iop = 14.77×10^{-3} A/cm^2 (Table 5). Although the as-built specimen has a lower *i*p than AA-2, the more extended passivation peak region indicates reduced corrosion resistance. However, a comparative analysis at E = 750 mV shows that AA-3 exhibits a higher current density than the as-built and AA-2 states (Table 5).

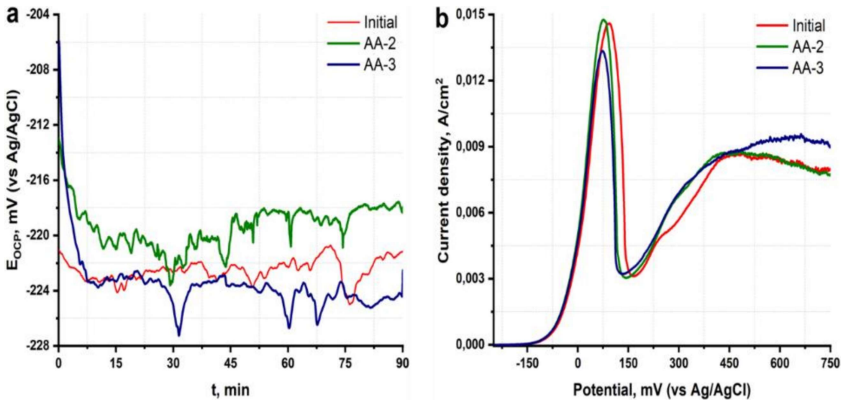

Figure 7. The open circuit potential (a) and anodic polarization curves of the Cu-Al-Ni alloys (b).

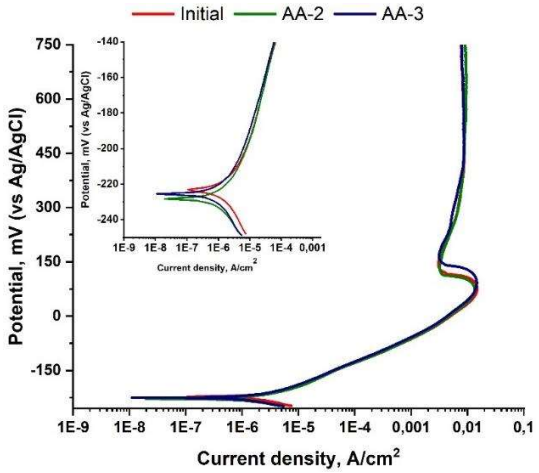

Figure 8. Potentiodynamic polarization curves of the Cu-Al-Ni alloys.

Examination of the Al-Cu-Ni alloy surface after corrosion testing revealed traces of localized corrosion (Figure 9) in all conditions. On the as-built specimen, the number and area of pits are higher (Figure 9a) than after heat treatment. According to the literature, the microstructure of Al-Cu-Ni alloys depends strongly on cooling rate and annealing temperature (Qin *et al*., 2018). Upon cooling, α-phase precipitates from the β-phase; concurrently or subsequently, the k_I phase (Fe_3Al) forms within the β-phase. Further cooling leads to the formation of the κ_{II} phase in the β-phase. At still lower temperatures, the κ_{IV} phase precipitates within the α-phase, and the remaining β-phase transforms into an α-phase containing κ_{III} inclusions. At high cooling rates, a β′-phase may form (Qin et al., 2018). The corrosion resistance of these phases differs substantially. For alloys of this class, a characteristic corrosion mode is selective phase corrosion, particularly when the heat treatment regime is not properly chosen.

All κ-phases are more corrosion-resistant than the α- and β′-phases. The latter two contain less aluminum, which otherwise promotes the formation of a protective oxide film. Wire-arc additive manufacturing (WAAM) to produce the Al-Cu-Ni alloy may have resulted in a high cooling rate, and consequently, the formation of β′-phase, which served as sites for initiating local corrosion. Corrosion products formed during dissolution, typically copper hydroxides, deposit on the surface, partially performing a protective function. In chloride-containing test solutions, CuCl forms on the surface and transforms into copper oxychloride, $Cu_2(OH)_3Cl$ (Yang et al., 2018).

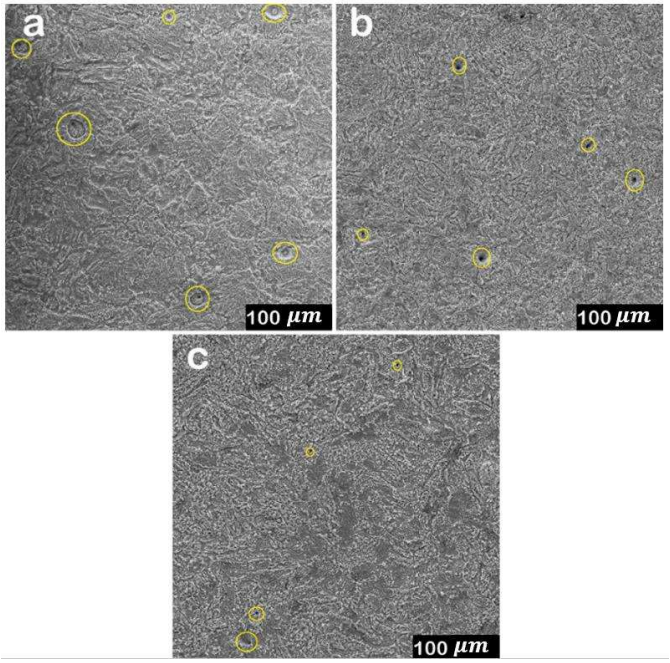

Figure 9. SE images of the sample surfaces after electrochemical corrosion testing: (a) as-built condition; (b) after AA-2 heat treatment; (c) after AA-3 heat treatment.

Elemental distribution maps of the as-built specimen surface after corrosion show that the corrosion products comprise several compounds (Figure 10). At pit centers, regions enriched in chlorine, oxygen, and copper are observed, consistent with $Cu_2(OH)_3Cl$. Parts of the pit surface are covered with aluminum and oxygen corrosion products. The corrosion of aluminum and its alloys is accompanied by the formation of sparingly soluble $Al(OH)_3$, which has protective

properties. When formed on the surface, it reduces the dissolution rate. Heat treatment yields a more equilibrated and homogenized structure, in which the principal alloying elements that enhance the corrosion resistance of NAB, such as Al and Ni, are distributed more uniformly, promoting a more uniform protective oxide film. Increasing the aging duration to 5 hours substantially reduces pit density on the surface (Figure 9c).

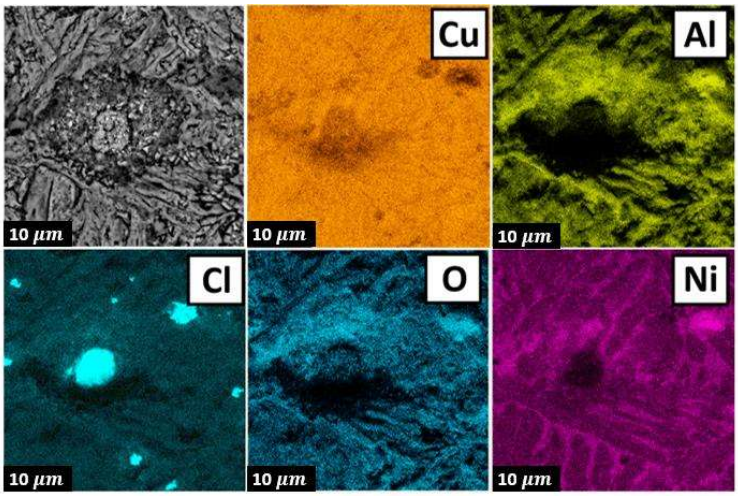

Figure 10. Elemental distribution maps in Cu-Al-Ni alloys in the as-built condition after corrosion tests.

Figure 11 shows the surface of the AA-2 specimen after corrosion testing and removal of corrosion products. Regions of the β-phase are more susceptible to corrosion, whereas the α-phase and intermetallic κ-phases exhibit virtually no traces of attack. The most likely reason for the selective corrosion of the β-phase in aluminum bronze is its enrichment in Al and Ni, which, on the one hand, should favor a more stable protective oxide/hydroxide film, but on the other hand, lowers the β-phase E_{corr}. In contact with the α and κ phases, β-phase areas become anodic and promote micro-galvanic corrosion.

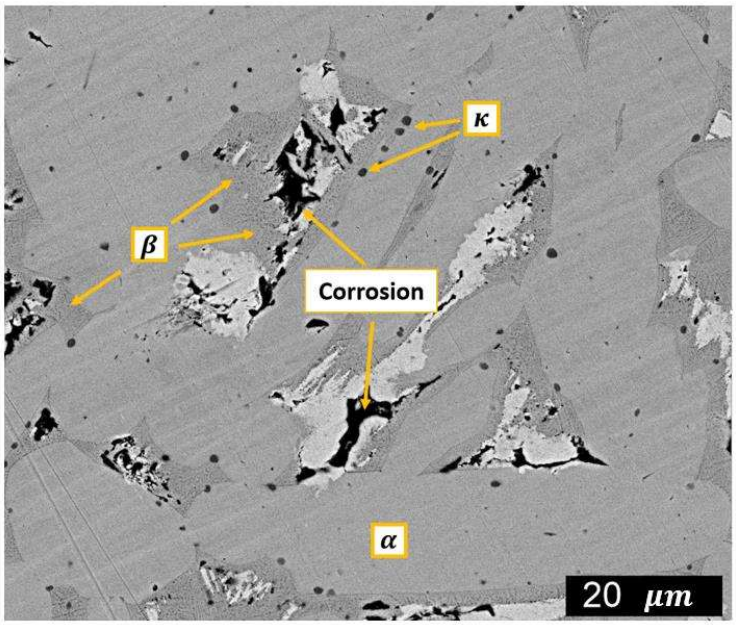

Figure 11. BSE image of the AA-2 surface after electrochemical corrosion testing and removal of corrosion products.

The obtained data indicate that the samples in the as-built condition and those subjected to various heat treatment regimes exhibit comparably high corrosion resistance. The polarization curves reveal a distinct passivation region at relatively high potentials and current densities. This behavior is attributed to the passivation of the alloy surface resulting from the formation of a protective Al_2O_3 film and the accumulation of corrosion products on the sample surface, which hinder further corrosion penetration into the bulk material. Similar observations were also reported by the reference authors (Ding *et al.*, 2016).

During the corrosion process, two main types of oxides, Cu_2O and Al_2O_3, form on the surface of the alloy. Cu_2O is not a protective oxide, as it has a porous structure and does not contribute to the passivation of the alloy. In contrast, Al_2O_3 is considered a more protective oxide; however, due to the relatively low aluminum content in these alloys, it cannot form a continuous and stable protective film at the early stages of corrosion. For a stable Al_2O_3 layer to develop on the alloy surface, a critical molar fraction of Al_2O_3 must first be reached. This can be achieved by increasing the aluminum content in the alloy or by enhancing the rate of copper dissolution from the surface. Since the aluminum content in the samples remains constant in this study, the passivation behavior of the alloy is governed solely by the rate of copper dissolution. It is also evident that different phases within the alloy exhibit varying rates of copper dissolution due to their distinct compositions and properties. This explains why a continuous aluminum oxide layer fails to form when the sample is immersed in seawater and covered by a film of corrosion products (Wharton *et al.*, 2005).

Despite the specific nature of the corrosion behavior of these alloys in seawater, their application as materials for marine propellers is justified by the relatively low rate of uniform corrosion observed in the early stages of exposure (approximately 0.04 mm/year). Furthermore, under conditions where an increase in anodic current density is observed at higher anodic overpotentials, these alloys undergo passivation due to the accumulation of Al_2O_3 on their surface, which contributes to extending their service life.

It can be observed that, in all samples, the eutectoid β phase enriched with Al and Ni is more susceptible to corrosion, whereas the Cu-rich solid solution cells, acting as cathodic sites, are less affected. This indicates the predominance of selective corrosion, a form of galvanic (contact) corrosion common in multiphase alloys. The primary driving force behind this type of corrosion is the difference in corrosion potential (E_{cor}) between the various phases of the alloy. As a result, galvanic coupling occurs between the phases, initiating the corrosion process. Nevertheless, despite selective corrosion, the overall depth of corrosion damage remains low. Corrosion proceeds relatively uniformly, without the development of deep pits typically observed in stainless steels such as 304 and 321. This behavior highlights a significant advantage of aluminum bronze over many austenitic stainless steels.

The samples that underwent heat treatment exhibited slightly higher i_{cor} than those in the as-built condition. This behavior is attributed to the increase in the proportion of the corrosive active β phase compared to the initial state. However, despite this, the E_p potential and density of pitting in samples AA-2 and AA-3 are lower than in the as-built state, which is associated with a better redistribution of chemical elements between phases after heat treatment and the formation of a more protective oxide layer.

Full-scale corrosion test

Figure 12 presents the results of seawater corrosion resistance tests for CuAl9Ni5 aluminum bronze produced using WAAM-CMT technology. Subsurface corrosion was observed in areas affected by biofouling, which is associated with disrupted aeration and the biological activity of marine organisms.

The most abundant fouling organisms were encrusting bryozoans and barnacles (*Amphibalanus* sp.). Bivalves (*Pinctada* sp. and possibly *Saccostrea* sp.), sponges, and tubeworms were also present. The most pronounced signs of corrosion were found in the

attachment sites of barnacles and sponges.After the removal of corrosion products, ulcerative-type corrosion damage became visible; however, it propagated primarily in the lateral direction with only limited depth, which reflects the characteristic corrosion mechanism of aluminum bronze. Deposits of elemental copper were detected within the corroded regions, attributed to the preferential dissolution of aluminum in these areas.

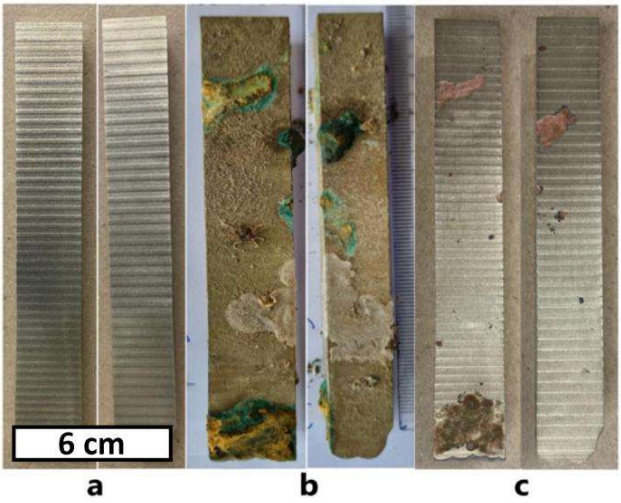

Figure 12. Appearance of the samples: (a) before testing; (b) after exposure in the as-built condition; (c) after exposure and removal of corrosion products and biofouling.

The protective Al_2O_3 film in areas affected by biofouling readily dissolves due to the aggressiveness of metabolic byproducts produced by marine organisms and regenerates poorly due to disrupted aeration. This leads to accelerated corrosion processes in biofouled zones compared to surfaces freely exposed to seawater flow. Furthermore, the progression of corrosion in these areas is also attributed to the accumulation of metabolic waste from marine organisms, which exerts a more aggressive chemical impact on the alloy surface.

It is evident that in areas free from biofouling, the alloy did not exhibit significant corrosion damage, with only uniform surface oxidation observed and no visible signs of localized attack. It is also noteworthy that biofouling tended to accumulate in regions with poor surface finish, which further reduced the corrosion resistance of the alloy. The corrosion rate was measured at 0.039 ± 0.005 g/m^2·h, corresponding to 0.046 ± 0.006 mm/year. The results obtained from laboratory testing of the $CuAl_9Ni_5$ alloy and field exposure show good agreement regarding the overall corrosion rate; however, the underlying corrosion mechanisms differ significantly.

Figure 13 presents SEM images of the samples from regions exhibiting maximum corrosion damage, along with the results of chemical analysis obtained via EDS. As observed, no pits or deep ulcerative features are present in these areas; instead, corrosion develops predominantly in the lateral direction with minimal penetration depth, which is considered an advantage of this alloy. The elemental distribution maps indicate a preferential dissolution of the eutectoid phase enriched with aluminum during corrosion in biofouling zones. In contrast, the α solid solution cells are less affected. This observation is consistent with the results obtained from laboratory-based corrosion testing. In the Al and O maps, these elements appear to be distributed relatively uniformly across the surface, allowing the conclusion that passivation occurs due to the formation of an Al_2O_3 layer. However, due to the high aggressiveness of the environment and impaired aeration in biofouling regions, this oxide layer does not provide complete protection, resulting in continued localized corrosion activity in these areas.

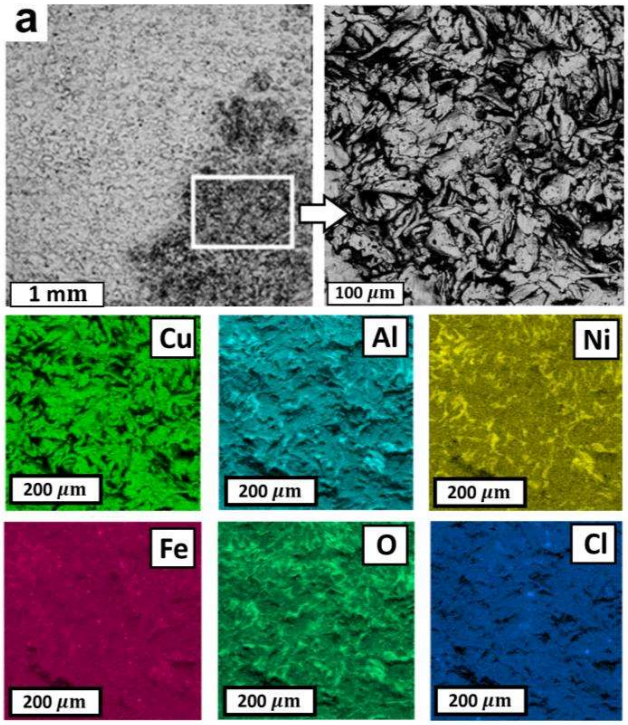

Figure 13. Microstructure of the alloy after full-scale seawater exposure: (a) SE image of the corrosion-affected region; (b) elemental distribution maps for Cu, Al, Ni, and Fe.

It is evident that, despite the high corrosion resistance of aluminum bronze in synthetic seawater, real-world field tests reveal the occurrence of biocorrosion caused by the activity of marine organisms. Under seawater exposure, biocorrosion poses a significant threat to alloys such as $CuAl_9Ni_5$ and represents a primary factor contributing to the premature failure of marine equipment.

Conclusion

This study examined the application of wire-arc additive manufacturing (WAAM) for producing nickel-aluminum bronze (NAB) $CuAl_9Ni_5$ components. In the as-built state, the microstructure consists of α-phase solid-solution cells with eutectoid β-phase regions between them and a small amount of κ-phase precipitates at the α/β phase boundaries. After heat treatment under the AA-2 and AA-3 regimes, the α-grains coarsen, the β-phase fraction increases, and κ-phase precipitates become larger and more numerous.

The fabricated NAB samples demonstrated excellent corrosion resistance, with attack remaining superficial and not penetrating significantly. The predominant corrosion mode is selective phase corrosion caused by micro-galvanic coupling among the α-, β-, and κ-phases, where the β-phase is anodic to the others owing to its higher Al and Ni contents. Heat treatment further reduces pit density, as more extended aging produces a more homogeneous microstructure.

Field tests in seawater corroborated the laboratory results on corrosion behavior. Moreover, it is evident that, under real operating conditions, the hazard arises from the aggressiveness of saline water and biocorrosion, which warrants further investigation.

After heat treatment, the mechanical properties change as follows: with increasing aging duration, the yield strength and ultimate tensile strength increase, while the elongation decreases. This is associated with a reduced fraction of the ductile α-phase in the alloy and an increased fraction of the stronger, harder κ- and β-phases.

A full-scale NAB propeller was successfully fabricated using the established WAAM

parameters. This study highlights the potential of WAAM technology for widespread adoption in industrial applications, confirming its feasibility for fabricating complex nickel-aluminum bronze components with enhanced performance characteristics.

Acknowledgments: *This work was financially supported by the Ministry of Science and Higher Education of the Russian Federation within the framework of the "World-class Science Center" program: Advanced digital technologies (Grant Agreement No. 075-15-2025-124, 31.03.2025). Corrosion tests in seawater were supported by the Joint Vietnam-Russia Tropical Science and Technology Research Center, the project "Ecolan T-2.2, Task 3".*

Statement on the use of Generative AI: *The authors declare that AI tools were used only for language editing/formatting, and not for generating scientific content. All data, analyses, and interpretations were performed and verified by the authors, who take full responsibility for the manuscript.*

Author contributions: *Shabunina Z.S., Uglunts T.V.: Conceptualization; Shabunina Z.S., Silkin A.O.: Methodology; Khalaman V.V., Gazizova M.Yu., Klimova-Korsmik O.G.: Formal analysis and investigation; Mendagaliev R.V., Shabunina S.S., Klimova-Korsmik O.G.: Writing - original draft preparation; Cao Nhat Linh, Nguyen Van Chi, Khalaman V.V., Gazizova M.Yu.: Writing - review and editing. All authors have read and agreed to the published version of the manuscript.*

Conflict of interest statement: *The authors declare that there are no conflicts of interest related to this article.*

References

Arcos, C., Ramos-Grez, J. A., Sancy, M., La Fé-Perdomo, I., Setchi, R., & Guerra, C. (2024). Suitability of nickel aluminium bronze alloy fabricated by laser powder bed fusion to be used in the marine environment. *Corrosion Science, 226*, 111656. https://doi.org/10.1016/j.corsci.2023.111656

Cai, X., Wang, Z., Dong, L., Yang, M., Zhou, J., & Xue, F. (2022). Advanced mechanical properties of nickel-aluminum bronze/steel composite structure prepared by wire-arc additive manufacturing. *Materials & Design, 221*, 110969. https://doi.org/10.1016/j.matdes.2022.110969

Cai, X., Yang, M., Qiao, Y., Wang, Z., Zhou, J., & Xue, F. (2023). Experimental investigation on wear resistance and corrosion behavior of nickel-aluminum bronze alloy fabricated by wire-arc additive manufacturing. *Journal of Materials Research and Technology*, *26*, 5801-5815. https://doi.org/10.1016/j.jmrt.2023.08.313

Cai, X., Yang, M., Wang, S., Wang, Z., Zhou, J., & Xue, F. (2023). Experimental investigations on corrosion behavior and antibacterial property of nickel-aluminum bronze fabricated through wire-arc additive manufacturing (WAAM). *Corrosion Science, 214*, 111040. https://doi.org/10.1016/j.corsci.2023.111040

Chalasani, D., & Mohammadi, M. (2023). Prospects of additively manufactured nickel aluminum bronzes for marine applications. In J. Kadkhodapour, S. Schmauder, & F. Sajadi (Eds.), *Quality analysis of additively manufactured metals* (pp. 627-687). Elsevier. https://doi.org/10.1016/B978-0-323-88664-2.00019-1

Chalasani, D., Amirkhiz, B. S., Lloyd, A., Ram, G. D. J., & Mohammadi, M. (2020). Wire-arc additive manufactured nickel aluminum bronze with enhanced mechanical properties using heat treatments cycles. *Additive Manufacturing, 36*, 101510. https://doi.org/10.1016/j.addma.2020.101510

Chalasani, D., Hadadzadeh, A., Amirkhiz, B. S., Ram, G. D. J., & Mohammadi, M. (2019). Microstructural evolution and mechanical behavior of nickel aluminum bronze Cu-9Al-4Fe-4Ni-1Mn fabricated through wire-arc additive manufacturing. *Additive Manufacturing, 30*, 100872. https://doi.org/10.1016/j.addma.2019.100872

Chalasani, D., Shakerin, S., Ram, G. J., & Mohammadi, M. (2020). Wire-arc additive manufacturing of nickel aluminum bronze/stainless steel hybrid parts-Interfacial characterization, prospects, and problems. *Materialia, 13*, 100834. https://doi.org/10.1016/j.mtla.2020.100834

Ding, D., Pan, Z., Van Duin, S., Li, H., & Shen, C. (2016). Fabricating superior NiAl bronze components through wire arc additive manufacturing. *Materials, 9*(8), 652. https://doi.org/10.3390/ma9080652

Govindaraj, R. B., Junghans, E., Andersen, I., Lim, Y. K., & Lindström, P. (2021). Additive manufactured marine component - NiAl bronze propeller. *Procedia Structural Integrity, 34*, 20-25. https://doi.org/10.1016/j.prostr.2021.12.039

Guo, X., Ma, M., Zhang, S., & Wei, Z. (2024). Microstructure and wear resistance of tungsten carbide particle reinforced titanium alloy coating by WAAM. *Tribology International, 194*, 109536. https://doi.org/10.1016/j.triboint.2024.109536

Kayvandarian, F., Zanganeh, D., Khodabakhshi, F., & Malekan, M. (2024). Corrosion properties of submerged friction stir modified as-cast nickel-aluminum bronze (NAB) compositions. *Electrochimica Acta, 501*, 144775. https://doi.org/10.1016/j.electacta.2024.144775

Korsmik, R., Tsybulskiy, I., Rodionov, A., Klimova-Korsmik, O., Gogolukhina, M., Ivanov, S., Zadykyan, G., & Mendagaliev, R. (2020). The approaches to design and manufacturing of large-sized marine machinery parts by direct laser deposition. *Procedia CIRP, 94*, 298-303. https://doi.org/10.1016/j.procir.2020.09.056

Liao, H., Kuang, Y., Zhou, D., Zhang, Q., Wu, X., Xu, L., Wang, X., & Wang, Z. (2024). Achieving fine-grained

structure with larger ferrite fraction via local dry underwater WAAM to enhance corrosion behavior of 308 L stainless steel. *Construction and Building Materials, 457*, 139510. https://doi.org/10.1016/j.conbuildmat.2024.139510

Liu, J., Miao, Y., Wang, Z., Zhao, Y., Wu, Y., & Li, C. (2024). Improved strength in nickel-aluminum bronze/steel bimetallic component fabricated using arcing-wire arc additive manufacturing with alternating deposition strategy. *Journal of Manufacturing Processes, 111*, 89-103. https://doi.org/10.1016/j.jmapro.2024.01.027

Liu, J., Miao, Y., Wei, C., Wang, Z., Zhao, Y., & Wu, Y. (2024). Enhanced mechanical properties in nickel-aluminium bronze alloy via wire arc additive manufacturing with follow-weld forced cooling. *Materials Characterization, 208*, 113653. https://doi.org/10.1016/j.matchar.2024.113653

Mendagaliev, R., Klimova-Korsmik, O., Promakhov, V., Schulz, N., Zhukov, A., Klimenko, V., & Olisov, A. (2020). Heat Treatment of Corrosion Resistant Steel for Water Propellers Fabricated by Direct Laser Deposition. *Materials (Basel, Switzerland)*, *13*(12), 2738. https://doi.org/10.3390/ma13122738

Orzolek, S. M., Semple, J. K., & Fisher, C. R. (2022). Influence of processing on the microstructure of nickel aluminum bronze (NAB). *Additive Manufacturing, 56*, 102859. https://doi.org/10.1016/j.addma.2022.102859

Qin, Z., Zhang, Q., Luo, Q., Wu, Z., Shen, B., Liu, L., & Hu, W. (2018). Microstructure design to improve the corrosion and cavitation corrosion resistance of a nickel-aluminum bronze. *Corrosion Science, 139*, 255-266. https://doi.org/10.1016/j.corsci.2018.04.043

Sarıkaya, M., Önler, D. B., Dağlı, S., Hartomacıoğlu, S., Günay, M., & Królczyk, G. M. (2024). A review on aluminum alloys produced by wire arc additive manufacturing (WAAM): Applications, benefits, challenges and future trends. *Journal of Materials Research and Technology*, *33*, 5643-5670. https://doi.org/10.1016/j.jmrt.2024.10.212

Shakil, S. I., Shakerin, S., Rahmdel, K., Mohammadi, M., Tridello, A., Paolino, D. S., Shao, S., Shamsaei, N., & Haghshenas, M. (2024). Fatigue response of wire-arc additive manufactured nickel-aluminum bronze (NAB) in the post-annealed condition. *International Journal of Fatigue*, 187, 108472. https://doi.org/10.1016/j.ijfatigue.2024.108472

Singh, S. R., & Khanna, P. (2021). Wire arc additive manufacturing (WAAM): A new process to shape engineering materials. *Materials Today: Proceedings, 44*(Part 1), 118-128.

https://doi.org/10.1016/j.matpr.2020.08.030

Song, Q. N., Zhang, H. N., Li, H. L., Hong, H., Sun, S. Y., Xu, N., Zhang, G. Y., Bao, Y. F., & Qiao, Y. X. (2022). Corrosion and cavitation erosion behaviors of the manganese-aluminum-bronze cladding layer prepared by MIG in 3.5% NaCl solution. *Materials Today Communications, 31*, 103566. https://doi.org/10.1016/j.mtcomm.2022.103566

Srivastava, M., Rathee, S., Tiwari, A., & Dongre, M. (2023). Wire arc additive manufacturing of metals: a review on processes, materials and their behaviour. *Materials Chemistry and Physics*, *294*, 126988. https://doi.org/10.1016/j.matchemphys.2022.126988

Wharton, J. A., Barik, R. C., Kear, G., Wood, R. J. K., Stokes, K. R., & Walsh, F. C. (2005). The corrosion of nickel-aluminium bronze in seawater. *Corrosion Science, 47*(12), 3336-3367. https://doi.org/10.1016/j.corsci.2005.05.053

Xu, C., Peng, Y., Chen, L. Y., Zhang, T. Y., He, S., & Wang, K. H. (2023). Corrosion behavior of wire-arc additive manufactured and as-cast Ni-Al bronze in 3.5 wt% NaCl solution. *Corrosion Science, 215*, 111048. https://doi.org/10.1016/j.corsci.2023.111048

Yang, F., Kang, H., Guo, E., Li, R., Chen, Z., Zeng, Y., & Wang, T. (2018). The role of nickel in mechanical performance and corrosion behaviour of nickel-aluminium bronze in 3.5 wt.% NaCl solution. *Corrosion Science, 139*, 333-345. https://doi.org/10.1016/j.corsci.2018.05.012

Zhang, Y., Yu, H., Wang, L., Wang, B., Su, B., Yao, L., Zhao, C., Cui, R., & Su, Y. (2024). Additive manufacturing nickel-aluminum bronze alloy via wire-fed electron beam directed energy deposition: Enhanced mechanical properties and corrosion resistance compared to as-cast counterpart. *Journal of Materials Research and Technology, 32*, 3871-3885. https://doi.org/10.1016/j.jmrt.2024.08.198

How to cite this article

Shabunina, Z. S., Uglunts, T. V., Silkin, A. O., Mendagaliev, R. V., Shabunina, S. S., Linh, C. N., Chi, N. V., Khalaman, V. V., Gazizova, M. Yu., & Klimova-Korsmik, O. G. (2026). *Microstructure, mechanical properties and corrosion behavior of nickel-aluminum bronze fabricated by wire-arc additive manufacturing*. *Journal of Tropical Science and Engineering, 1*(2), 45-59. https://doi.org/10.58334/jtse.vol.001.795